

Optics Letters

All-optical neuromorphic XOR operation with inhibitory dynamics of a single photonic spiking neuron based on a VCSEL-SA

SHUIYING XIANG,^{1,2,*} ZHENXING REN,¹ YAHUI ZHANG,¹ ZIWEI SONG,¹ AND YUE HAO²

¹State Key Laboratory of Integrated Service Networks, Xidian University, Xi'an 710071, China

²State Key Discipline Laboratory of Wide Bandgap Semiconductor Technology, School of Microelectronics, Xidian University, Xi'an 710071, China

*Corresponding author: jxxy@126.com

Received 21 November 2019; revised 30 December 2019; accepted 13 January 2020; posted 15 January 2020 (Doc. ID 383942); published 19 February 2020

We propose a simple hardware architecture for solving exclusive OR (XOR) tasks in a single step by using a single photonic spiking neuron based on vertical-cavity surface-emitting lasers with an embedded saturable absorber (VCSEL-SA) subject to dual-polarized pulsed optical injection. We model the inhibitory photonic spiking neuron by extending the Yamada model and spin-flip model to incorporate the two polarization-resolved modes and the saturable absorber. It is shown that, by carefully adjusting the temporal difference according to the inhibitory window, the XOR operation can be realized in a single photonic spiking neuron, which is interesting and valuable for the photonic neuromorphic computing and information processing. © 2020 Optical Society of America

<https://doi.org/10.1364/OL.383942>

The developments of deep learning and big data techniques have revolutionized a wide range of applications such as image processing, autonomous driving, and pattern recognition. They have also raised significant challenges for hardware implementations in terms of computation, memory, and communication resources. The conventional computing based on the von Neumann architecture faces memory and power consumption bottlenecks. To overcome these limitations, neuro-inspired computing systems beyond the von Neumann architecture have made remarkable milestones [1–4]. As an alternative hardware platform, photonics neuromorphic computing systems have emerged in recent years due to the promising improvements in both speed and energy efficiency over conventional electronics approaches [5–12].

At the device level, intensive research efforts have been devoted to emulate the spiking dynamics of biological neurons [13–18]. Note that both excitatory and inhibitory dynamics are critical for the neural information processing. In photonic signal processing, the use of power envelopes to represent signals raises challenges in producing inhibitory and excitatory responses. With the help of optical-to-electrical conversion, the inhibitory dynamics has been demonstrated by using balanced

photodetectors [6]. In addition, some novel all-optical schemes and mechanisms have been proposed to emulate the inhibitory dynamics [19–23]. Recently, Robertson *et al.* reported controllable inhibitory dynamics in a vertical-cavity surface-emitting laser (VCSEL) based on polarization switching [19]. Besides, controlled generation and inhibition of externally triggered picosecond optical pulsating regimes were demonstrated experimentally in a quantum dot mode-locked laser [21]. We previously predicted the inhibitory dynamics based on the polarization mode competition (PMC) effect in a VCSEL with an embedded saturable absorber (VCSEL-SA), in which a well-defined inhibition window could be observed and could be further adjusted by changing the injection current [23].

Furthermore, at the system level, photonic spike processing circuits, photonic spiking neural network (SNN), and machine learning based on neuromorphic photonics have also been explored both experimentally and theoretically [7–12]. For example, Feldmann fabricated an all-optical neural network consisting of four neurons and 60 synapses on a nanophotonic chip, which was capable of performing pattern recognition with unsupervised learning or supervised learning algorithms [8]. In our previous work, we presented a unified computational model and simulation framework for device-algorithm co-design of the photonic SNN consisting of VCSELs-SA [9]. Usually, to solve complex tasks, a multi-layer SNN is required. For instance, Peng *et al.* proposed a method to implement exclusive OR (XOR) classification using a photonic SNN consisting of three integrated laser neurons [12]. Besides, the conventional all-optical XOR operators based on semiconductor optical amplifiers (SOAs), usually require relatively high power, multiple steps, or more than one SOA [24,25]. However, a very promising approach for XOR operation is based on VCSELs, as they have been shown to exhibit excitatory and inhibitory dynamics and rich polarization dynamics, and are more energy-efficient compared to the counterparts. To the best of our knowledge, a dedicated VCSEL-based photonic SNN for XOR operation has not yet been addressed.

In this Letter, we propose a simple hardware structure for solving the XOR problem in a single step by using a single

photonic spiking neuron based on a VCSEL-SA subject to dual-polarized pulsed optical injection (DPPOI). The VCSEL-SA is assumed to support both x-polarization (XP) and y-polarization (YP) modes. The underlying mechanisms and operating conditions are revealed through numerical simulation based on a theoretical model that combines both the spin-flip model and Yamada model.

The schematic diagram of the proposed XOR operator based on a single photonic spiking neuron is presented in Fig. 1. At first, the two input bits are pre-encoded into temporal information. Here, the bit 0 (1) is encoded into t_a (t_b). t_a and t_b denote the central timing of an optical rectangle pulse with width being 2 ns. For convenience, we consider $t_a < t_b$. Then the optical rectangle pulse corresponding to In 1 (In 2) is injected into the XP (YP) mode of a VCSEL-SA. Importantly, two different delay lines ($\Delta\tau_x$ and $\Delta\tau_y$) are required for successful XOR operation. After that, the external stimulus pulse arrives at the XP (YP) mode of the VCSEL-SA at $t_x = t_{a,b} + \Delta\tau_x$ ($t_y = t_{a,b} + \Delta\tau_y$). The XOR output can be realized by the spiking dynamics of the VCSEL-SA with DPPOI.

The theoretical model of a VCSEL-SA subject to DPPOI is derived based on the combination of the spin-flip model and Yamada model [23,26–28]:

$$\begin{aligned} \frac{dF_x}{dt} = & \frac{1}{2}(1+i\alpha)[(D_1+D_2-1)F_x + i(d_1+d_2)F_y] \\ & - (\varepsilon_a + i\varepsilon_p)F_x + k_{injx}F_{injx}(t + \Delta\tau_x)e^{i\Delta\omega_x t} \\ & + \sqrt{\beta_{sp}}\xi_x, \end{aligned} \quad (1)$$

$$\begin{aligned} \frac{dF_y}{dt} = & \frac{1}{2}(1+i\alpha)[(D_1+D_2-1)F_y - i(d_1+d_2)F_x] \\ & + (\varepsilon_a + i\varepsilon_p)F_y + k_{in jy}F_{in jy}(t + \Delta\tau_y)e^{i\Delta\omega_y t} \\ & + \sqrt{\beta_{sp}}\xi_y, \end{aligned} \quad (2)$$

$$\begin{aligned} \dot{D}_{1,2} = & \gamma_{1,2}[\mu_{1,2} - D_{1,2} - \frac{1}{2}a_{1,2}(D_{1,2} + d_{1,2})|F_x - iF_y|^2 \\ & - \frac{1}{2}a_{1,2}(D_{1,2} - d_{1,2})|F_x + iF_y|^2 + c_{12,21}D_{2,1}], \end{aligned} \quad (3)$$

$$\begin{aligned} \dot{d}_{1,2} = & -\gamma_{s1,2}d_{1,2} - \gamma_{1,2}[\frac{1}{2}a_{1,2}(D_{1,2} + d_{1,2})|F_x - iF_y|^2 \\ & - \frac{1}{2}a_{1,2}(D_{1,2} - d_{1,2})|F_x + iF_y|^2 - c_{12,21}d_{2,1}], \end{aligned} \quad (4)$$

where F_x and F_y account for the slowly varying complex amplitudes of the two polarization-resolved modes, i.e., XP and YP

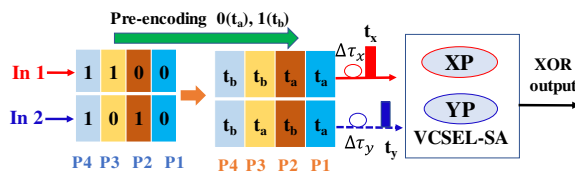


Fig. 1. Schematic diagram of the proposed XOR operator based on a VCSEL-SA subject to DPPOI.

modes. The subscript 1 (2) denotes the gain (saturable absorber) region. $D_{1,2}$ describe the total carrier inversion between the conduction and valence bands related to the transparency carrier density. $d_{1,2}$ represent the carrier inversions with opposite spin orientations. The DPPOI are represented by F_{injx} ($F_{in jy}$) denoting the optical rectangle pulse that is injected into the XP (YP) mode, as well as angular frequency differences $\Delta\omega_x$ and $\Delta\omega_y$. k_{injx} and $k_{in jy}$ denote the injection strengths. ε_a (ε_p) is the amplitude (phase) anisotropy. $c_{12}D_2$ and $c_{21}D_1$ are the carrier diffusion. α is the linewidth enhancement factor, $\gamma_{1,2}$ are the total carrier decay rates, and $\gamma_{s1,2}$ are the spin-flip rates. $\mu_{1,2}$ are the injection currents. $a_{1,2}$ are the differential gains. Here, we define $\varepsilon_p = \gamma_p/\kappa$, where γ_p denotes the birefringence, and κ is the cavity decay rate. The equations are written in a dimensionless form, so the time is measured in units of κ^{-1} . The following parameter values are fixed in simulation [23,26–28]: $\alpha = 3$, $\mu_1 = 2.1$, $\mu_2 = -6.1$, $\varepsilon_a = 0$, $\gamma_1 = 1.09 \times 10^{-3}$, $\gamma_2 = 1.13 \times 10^{-3}$, $\gamma_{s1} = \gamma_{s2} = 0.25$, $\gamma_p = 15 \text{ ns}^{-1}$, $\kappa = 390 \text{ ns}^{-1}$, $k_{injx} = k_{in jy} = 1.3$, $\Delta\omega_x = \Delta\omega_y = 0 \text{ rad/s}$, $a_1 = 1$, $a_2 = 8.7$, $c_{12} = 2.84 \times 10^{-2}$, and $c_{21} = 1.91$, unless otherwise stated. With these parameters, the lasing threshold of the VCSEL-SA is $\mu_{th} = 2.6$.

To begin, we consider a simple case to show the inhibitory dynamics of the photonic spiking neuron based on a VCSEL-SA with DPPOI. The central timing of $F_{in jy}$ is fixed at $t_y = 47 \text{ ns}$. The central timing of F_{injx} is considered as a variable that ranges from $t_x = 47 \text{ ns}$ to $t_x = 57 \text{ ns}$. The response dynamics of two polarization-resolved modes is shown in Figs. 2(a) and 2(b). Here, the intensities are calculated by $I_x = |F_x|^2$ and $I_y = |F_y|^2$. The maximum values of $I_{xm} = \max(I_x)$ and $I_{ym} = \max(I_y)$ as functions of t_x are also presented in Figs. 2(c) and 2(d). It can be seen that, when $t_x < t_y$, namely, F_{injx} is applied before $F_{in jy}$, as presented in the left part of Fig. 2(a), an output spike with maximal amplitude is generated for each case of t_x . Moreover, I_{xm} keeps at a constant, as this output spike is triggered by the preceding stimulus pulse. Simultaneously, I_{ym} decreases gradually to a negligible level due to the PMC effect. On the other hand, when $t_x > t_y$, especially when two stimuli pulses which are close in time are applied to the VCSEL-SA, the response in the XP mode is inhibited, and I_{xm} is close to 0. As denoted by the shading region in Fig. 2(a), we define the width of the inhibition window as $\tau_{inh} = 3 \text{ ns}$. For convenience, we consider that the response is inhibited when $I_{xm} < 20$ [23]. When t_x is further increased, the value of I_{xm} increases gradually due to the carrier recovery process. Note that the width of the inhibition window can be controlled by varying the injection current [23].

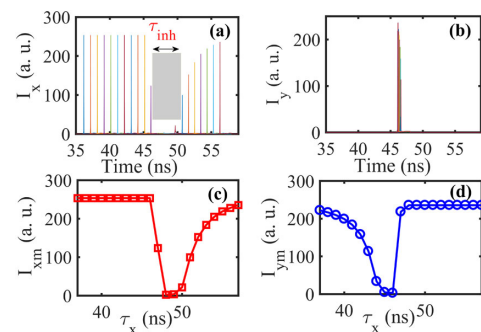


Fig. 2. Inhibitory dynamics of a VCSEL-SA subject to DPPOI.

Next, we explore the XOR operation based on the proposed architecture. Here, we consider four input patterns, 00(P1), 01(P2), 10(P3), and 11(P4); the corresponding XOR results are 0, 1, 1, and 0.

To realize XOR output in the XP mode by using the inhibitory dynamics, the temporal difference should be wisely selected. When two inputs are the same (P1 or P4), the following condition should be fulfilled to ensure that only YP mode emits a spike:

$$0 < t_x - t_y < \tau_{inh}. \quad (5)$$

When two inputs are different (P2 or P3), the following condition should be satisfied to enable spike emission in the XP mode:

$$t_x - t_y > \tau_{inh} \quad \text{or} \quad t_x - t_y < 0. \quad (6)$$

To this end, we reveal the design rule for XOR operation via the XP mode as follows:

$$0 < \Delta\tau_x - \Delta\tau_y < \tau_{inh} \quad \text{and} \quad (t_b - t_a) + (\Delta\tau_x - \Delta\tau_y) > \tau_{inh}. \quad (7)$$

Specifically, the bit 0 (1) is pre-encoded to $t_a = 47$ ns ($t_b = 57$ ns). We fix $\Delta\tau_x = 1$ ns, $\Delta\tau_y = 0$. Under this condition, the stimulus pulse and the response in two polarization-resolved modes are shown in Fig. 3. It can be found that, for P1, $t_x = t_a + \Delta\tau_x = 48$ ns, $t_y = t_a + \Delta\tau_y = 47$ ns, the YP mode emits a spike due to the preceding stimulus pulse and depletes the carriers. As $0 < t_x - t_y < \tau_{inh}$, the stimulus pulse arriving at the XP mode is shortly after that arriving at the YP mode (in the inhibition window), the XP mode cannot emit a spike due to the PMC effect. For P2, $t_x = 48$ ns, $t_y = 57$ ns, the preceding stimulus pulse triggers a spike emission in the XP mode. As $t_y - t_x > \tau_{inh}$, the lagging stimulus pulse arriving can also trigger a spike in the YP mode due to the carrier recovery process. For P3, $t_x = 58$ ns, $t_y = 47$ ns. Similarly, both XP and YP modes can emit a spike upon the stimulus pulse. For P4, $t_x = 58$ ns, $t_y = 57$ ns, only a YP mode emits a spike. Interestingly, we find that, with or without spike emission, the XP mode is exactly the XOR result. More precisely, when the XP mode emits a spike, the XOR result can be regarded as 1. Otherwise, the XOR result is 0. Hence, both the inhibitory dynamics and the carrier recovery process are responsible for the XOR operation.

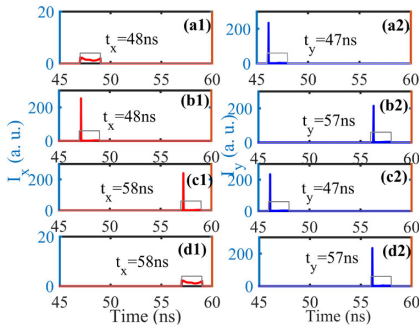


Fig. 3. XOR output in the XP mode for different sets of input with (a1, a2) 00, (b1, b2) 01, (c1, c2) 10, and (d1, d2) 11. The dashed lines indicate the external stimulation of the optical rectangle pulse after the delay lines.

Note that as illustrated in Fig. 2, when the stimulus pulse arrives at the XP mode earlier, it will also inhibit the emission of spikes in the YP mode in an inhibition window. Correspondingly, the spike emission in the YP mode can also be employed for the XOR operation, provided the following design rule is satisfied:

$$0 < \Delta\tau_y - \Delta\tau_x < \tau_{inh} \quad \text{and} \quad (t_b - t_a) + (\Delta\tau_y - \Delta\tau_x) > \tau_{inh}. \quad (8)$$

For the case of $\Delta\tau_y = 1$ ns, $\Delta\tau_x = 0$, the XOR output is shown in Fig. 4. It can be seen that, under this specific condition, the XOR result can also be achieved by the spike emission in the YP mode.

Subsequently, we focus on the output of the XP mode and consider two sets of pseudo-random return-to-zero (RZ) sequences as two inputs. The period of the RZ sequence is set as $T = 10$ ns. In the M th period, the bit 0 (1) is pre-encoded into $t_a = M \times T$ ($t_b = M \times T + 5$ ns). One representative case is depicted in Fig. 5. The temporal code for the XP injection is 25, 30, 40, 55, 65, 75, 80, 90, 105, and 110 ns. The temporal code for the YP injection is 25, 35, 40, 50, 65, 70, 85, 95, 105, and 110 ns. It is verified that the spike emission of the XP mode is consistent with the XOR result. In other words, the XP mode with (without) spike emission corresponds to the XOR result of 1 (0).

Without loss of generality, we also consider the robustness of XOR operation to noise and time jitter. As can be seen in Fig. 6, the XOR operation is robust to noise when the signal-to-noise ratio (SNR) = 20 dB. The role of time jitter on the XOR operation is further shown in Fig. 7. For clarity, only six bits are shown here. The temporal code with random time jitter for the XP injection is 65.35, 74.82, 79.21, 90.14, 104.33, and 110.18 ns. Correspondingly, the temporal code for the YP injection is 63.97, 69.59, 85.25, 95.02, 105.56, and 109.85 ns.

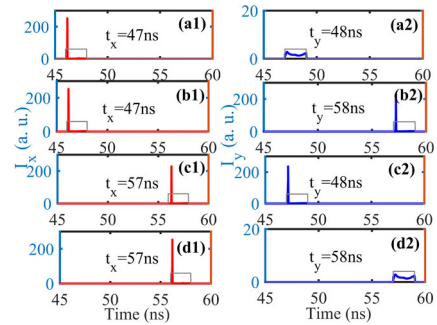


Fig. 4. Same as in Fig. 3 but for the XOR output in the YP mode.

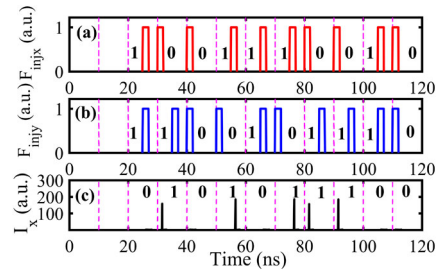


Fig. 5. (a) and (b) correspond, respectively, to the RZ input into the XP and YP modes; (c) the XOR output for two RZ sequences. With $\Delta\tau_x = 1$ ns, $\Delta\tau_y = 0$.

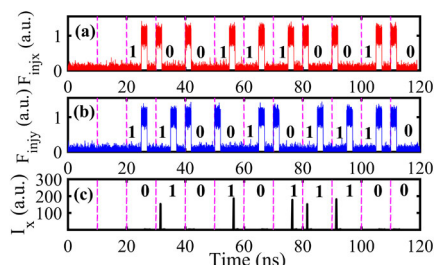


Fig. 6. XOR output for two RZ sequences with SNR = 20 dB.

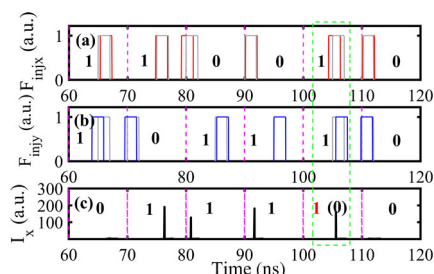


Fig. 7. XOR output for two RZ sequences with random time jitters. The original temporal codes for both XP and YP injections are the same as those in Fig. 6.

As indicated in the dashed box in Fig. 7, for the 5th input, $t_x = t'_b + \Delta\tau_x = 105.33$ ns, $t_y = t'_b + \Delta\tau_y = 105.56$ ns, the condition illustrated in Eq. (5) is not fulfilled because the time jitter is too large, and the XOR result is wrong. For the rest of the cases, the XOR output can be achieved as long as the XOR condition highlighted in Eqs. (5) and (6) is satisfied. Hence, the XOR operation is robust to small time jitter.

At last, we also examined the effects of bias current and frequency detuning. It is found that the XOR operation can be achieved for different injection currents and is robust to small frequency detuning (not shown here). It is worth mentioning that different injection currents lead to different inhibition windows. Therefore, the operating range represented by the mentioned conditions will be different.

In summary, we propose a simple hardware architecture to perform the neuromorphic XOR operation in a single step by using a single photonic spiking neuron based on a VCSEL-SA subject to DPPOI. The operating condition and underlying mechanisms are revealed. It is found that, with the time difference of the temporal encoding for two different bits, and the connection delays are carefully adjusted according to the inhibition window, the XOR operation can be achieved through the spike emission of the polarization-resolved mode. The inhibitory dynamics based on the PMC and the carrier recovery process are two main factors that determine the XOR operation. To the best of our knowledge, this is the first time that the spike-based XOR operation is realized in a single step with a single VCSEL-SA, which shows promise in the energy-efficient photonic neuromorphic computing and neuromorphic information processing, and may further motivate other spike-based logic operators based on the VCSEL-SA.

Funding. National Natural Science Foundation of China (61974177, 61674119); Postdoctoral innovation talent

program in China (BX201600118); China Postdoctoral Science Foundation (2017M613072); Postdoctoral Science Foundation in Shaanxi Province of China.

Disclosures. The authors declare no conflicts of interest.

REFERENCES

- P. A. Merolla, J. V. Arthur, R. Alvarez-Icaza, A. S. Cassidy, J. Sawada, F. Akopyan, B. L. Jackson, N. Imam, C. Guo, Y. Nakamura, B. Brezzo, I. Vo, S. K. Esser, R. Appuswamy, B. Taba, A. Amir, M. D. Flickner, W. P. Risk, R. Manohar, and D. S. Modha, *Science* **345**, 668 (2014).
- M. Prezioso, F. Merrikh-Bayat, B. D. Hoskins, G. C. Adam, K. K. Likharev, and D. B. Strukov, *Nature* **521**, 61 (2015).
- C. D. Schuman, T. E. Potok, R. M. Patton, J. D. Birdwell, M. E. Dean, G. S. Rose, and J. S. Plank, "A survey of neuromorphic computing and neural networks in hardware," arXiv:1705.06963 (2017).
- J. Pei, L. Deng, S. Song, M. G. Zhao, Y. H. Zhang, S. Wu, G. R. Wang, Z. Zou, Z. Z. Wu, W. He, F. Chen, N. Deng, S. Wu, Y. Wang, Y. J. Wu, Z. Y. Yang, C. Ma, G. Q. Li, W. T. Han, H. L. Li, H. Q. Wu, R. Zhao, Y. Xie, and L. P. Shi, *Nature* **572**, 106 (2019).
- P. R. Prucnal, B. J. Shastri, T. F. de Lima, M. A. Nahmias, and A. N. Tait, *Adv. Opt. Photonics* **8**, 228 (2016).
- H. T. Peng, M. A. Nahmias, T. Ferreira de Lima, A. N. Tait, B. J. Shastri, and P. R. Prucnal, *IEEE J. Sel. Top. Quantum Electron.* **24**, 6101715 (2018).
- T. F. de Lima, H.-T. Peng, A. N. Tait, M. A. Nahmias, H. B. Miller, B. J. Shastri, and P. R. Prucnal, *J. Lightwave Technol.* **37**, 1515 (2019).
- J. Feldmann, N. Youngblood, C. D. Wright, H. Bhaskaran, and W. H. P. Pernice, *Nature* **569**, 208 (2019).
- S. Y. Xiang, Y. Zhang, J. Gong, X. Guo, L. Lin, and Y. Hao, *IEEE J. Sel. Top. Quantum Electron.* **25**, 1700109 (2019).
- V. A. Pammi, K. Alfaro-Bittner, M. G. Clerc, and S. Barbay, *IEEE J. Sel. Top. Quantum Electron.* **26**, 1500307 (2020).
- J. Robertson, E. Wade, Y. Kopp, J. Bueno, and A. Hurtado, *IEEE J. Sel. Top. Quantum Electron.* **26**, 7700715 (2020).
- H.-T. Peng, G. Angelatos, T. Ferreira de Lima, M. A. Nahmias, A. N. Tait, S. Abbaslou, B. J. Shastri, and P. R. Prucnal, *IEEE J. Sel. Top. Quantum Electron.* **26**, 5100209 (2020).
- A. Hurtado, I. D. Henning, and M. J. Adams, *Opt. Express* **18**, 25170 (2010).
- S. Barbay, R. Kuszelewicz, and A. M. Yacomotti, *Opt. Lett.* **36**, 4476 (2011).
- A. Hurtado, K. Schires, I. D. Henning, and M. J. Adams, *Appl. Phys. Lett.* **100**, 103703 (2012).
- M. A. Nahmias, B. J. Shastri, A. N. Tait, and P. R. Prucnal, *IEEE J. Sel. Top. Quantum Electron.* **19**, 1800212 (2013).
- F. Selmi, R. Braive, G. Beaudoin, I. Sagnes, R. Kuszelewicz, and S. Barbay, *Phys. Rev. Lett.* **112**, 183902 (2014).
- S. Xiang, Y. Zhang, X. Guo, A. Wen, and Y. Hao, *J. Lightwave Technol.* **36**, 4227 (2018).
- J. Robertson, T. Deng, J. Javaloyes, and A. Hurtado, *Opt. Lett.* **42**, 1560 (2017).
- P. Y. Ma, B. J. Shastri, T. F. de Lima, C. Huang, A. N. Tait, M. A. Nahmias, H.-T. Peng, and P. R. Prucnal, *Opt. Lett.* **43**, 3802 (2018).
- J. Robertson, T. Ackemann, L. F. Lester, and A. Hurtado, *Sci. Rep.* **8**, 12515 (2018).
- T. Deng, J. Robertson, Z. Wu, G. Xia, X. Lin, X. Tang, Z. Wang, and A. Hurtado, *IEEE Access* **6**, 67951 (2018).
- Y. Zhang, S. Y. Xiang, X. Guo, A. Wen, and Y. Hao, *Opt. Lett.* **44**, 1548 (2019).
- J.-Y. Kim, J.-M. Kang, T.-Y. Kim, and S.-K. Han, *J. Lightwave Technol.* **24**, 3392 (2006).
- A. E. Willner, S. Khaleghi, M. R. Chitgarha, and O. F. Yilmaz, *J. Lightwave Technol.* **32**, 660 (2014).
- A. Scirè, J. Mulet, C. R. Mirasso, and M. San Miguel, *Opt. Lett.* **27**, 391 (2002).
- K. Panajotov and M. Tliidi, *Opt. Lett.* **43**, 5663 (2018).
- Y. H. Zhang, S. Y. Xiang, X. X. Guo, A. J. Wen, and Y. Hao, *Sci. Rep.* **8**, 16095 (2018).